Impact of atmospheric forcing on Antarctic continental shelf water masses

Impact of Atmospheric Forcing on Antarctic Continental Shelf Water Masses

ALEK A. PETTY

Centre for Polar Observation and Modelling, Department of Earth Sciences, University College London, London, United Kingdom

DANIEL L. FELTHAM

Centre for Polar Observation and Modelling, Department of Meteorology, University of Reading, Reading, United Kingdom

PAUL R. HOLLAND

British Antarctic Survey, Cambridge, United Kingdom

(Manuscript received 14 September 2012, in final form 1 November 2012)

ABSTRACT

The Antarctic continental shelf seas feature a bimodal distribution of water mass temperature, with the Amundsen and Bellingshausen Seas flooded by Circumpolar Deep Water that is several degrees Celsius warmer than the cold shelf waters prevalent in the Weddell and Ross Seas. This bimodal distribution could be caused by differences in atmospheric forcing, ocean dynamics, ocean and ice feedbacks, or some combination of these factors. In this study, a highly simplified coupled sea ice–mixed layer model is developed to investigate the physical processes controlling this situation. Under regional atmospheric forcings and parameter choices the 10-yr simulations demonstrate a complete destratification of the Weddell Sea water column in winter, forming cold, relatively saline shelf waters, while the Amundsen Sea winter mixed layer remains shallower, allowing a layer of deep warm water to persist. Applying the Weddell atmospheric forcing to the Amundsen Sea model destratifies the water column after two years, and applying the Amundsen forcing to the Weddell Sea model results in a shallower steady-state winter mixed layer that no longer destratifies the water column. This suggests that the regional difference in atmospheric forcings alone is sufficient to account for the bimodal distribution in Antarctic shelf-sea temperatures. The model prediction of mixed layer depth is most sensitive to the air temperature forcing, but a switch in all forcings is required to prevent destratification of the Weddell Sea water column.

1. Introduction

The continental shelf seas surrounding Antarctica show a clear bimodal distribution in the temperature of the ocean at the seabed (Fig. 1). The Weddell and Ross shelf seas are filled with cold, saline, oxygen-rich shelf waters at around the surface freezing temperature (−1.9°C) (Jacobs et al. 1970; Gill 1973; Nicholls et al. 2009; Orsi and Wiederwohl 2009), while the Amundsen and Bellingshausen shelf seas are flooded with Circumpolar Deep Water (CDW), which is warm (+1°C), slightly less saline, and deoxygenated (Talbot 1988; Hellmer et al. 1998; Jenkins and Jacobs 2008; Martinson et al. 2008; Jacobs et al. 2011). Both the Weddell and Ross Seas are influenced by strong katabatic winds (van Lipzig et al. 2004), resulting in low air temperatures and the formation of persistent coastal polynyas. For this study the southwestern Weddell shelf sea is chosen as the representative cold shelf sea region as it is the source of the coldest and most voluminous bottom water (Gordon et al. 2010), and because we have better access to oceanographic data and expertise of the region. We also expect the atmospheric conditions over the Amundsen and Bellingshausen shelf seas to be similar, and in this case the Amundsen shelf sea is chosen as the representative warm shelf sea region as it is an area of current scientific focus with the rapid thinning of Pine Island Glacier (Jacobs et al. 2011).

Corresponding author address: Alek A. Petty, National Centre for Earth Observation, Centre for Polar Observation and Modelling, Department of Earth Sciences, University College London, London, WC1E 6BT, United Kingdom.
E-mail: alek.petty.10@ucl.ac.uk

DOI: 10.1175/JPO-D-12-0172.1

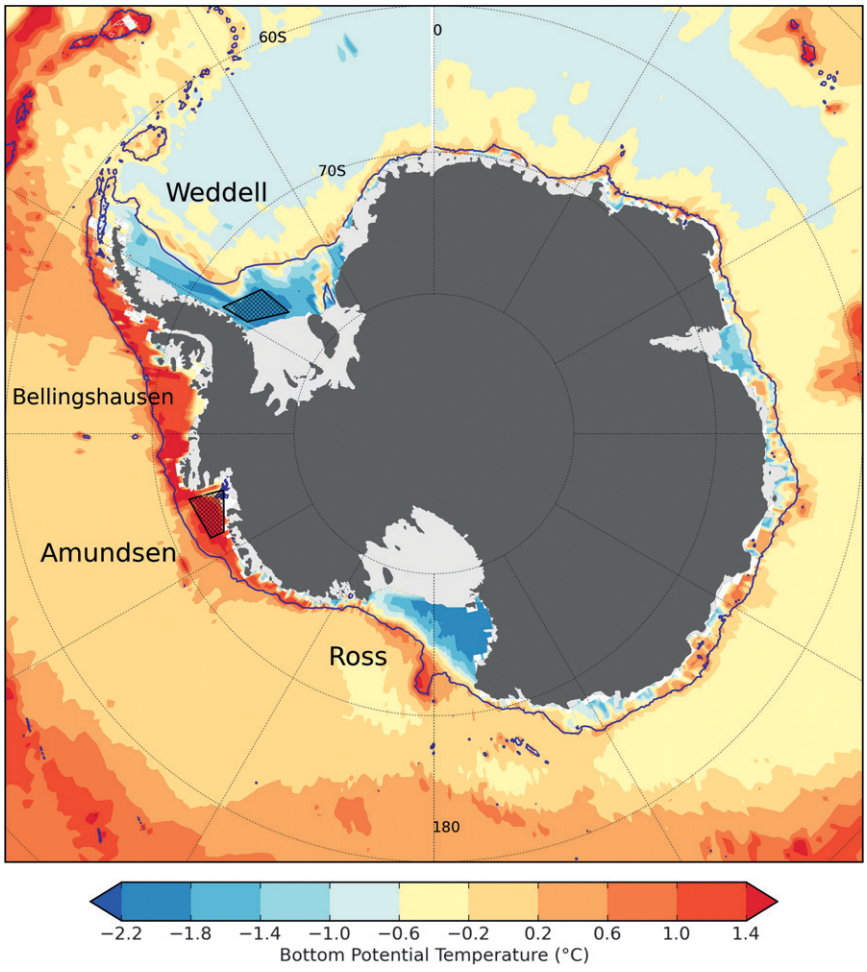

FIG. 1. Map of the Southern Ocean bottom potential temperature. Ocean data are from the WOCE global hydrographic climatology (Gouretski and Koltermann 2004). The reference study regions are shown by the black hatched boxes in the Weddell and Amundsen seas. The 1000-m bathymetry contour (dark blue line) and the Antarctic landmask are taken from the RTOPO dataset (Timmermann et al. 2010).

In the Weddell Sea, brine rejection during winter sea ice growth results in the formation of high salinity shelf water (HSSW), as interaction with the atmosphere progressively cools and salinates the sea surface until the negative buoyancy flux mixes the entire water column and the surface mixed layer can be regarded as extending to the seabed. This process is strongest in the coastal polynya in the southwestern corner of the Weddell Sea. However, the winter heat loss through the polynya provides only a small fraction (around 10%) of the heat loss needed to convert the summertime shelf waters into HSSW (Renfrew et al. 2002; Nicholls et al. 2009). The gradual brine flux from the more extensive pack ice is therefore thought to be the principal mechanism for creating HSSW in the Weddell Sea and is the process that we are most concerned with in this study. This HSSW either crosses the shelf break to the north or enters the Ronne cavity to the south, producing ice shelf water (ISW) as the HSSW melts the base of the Filchner–Ronne Ice Shelf (FRIS). Most of this ISW is thought to be transported off the continental shelf via the Filchner Depression (Foldvik et al. 2004; Wilchinsky and Feltham 2009), along with a smaller fraction emerging at various locations along the Ronne ice front. $\delta_{18}O$ data from Nicholls et al. (2003) show that none of the HSSW entering the cavity is reconverted ISW. It is therefore expected that ISW does not contribute much to the properties of the water in the southwestern Weddell shelf sea. North of the continental shelf, warm CDW enters at the northeastern corner of the Weddell Gyre and mixes with cold surface waters to produce warm deep water (WDW) (Fahrbach et al. 1994). Below the WDW is Weddell Sea Deep Water (WSDW), an intermediate water mass that can be regarded as the Weddell

Sea component of Antarctic Bottom Water (AABW) (Foldvik et al. 1985), the densest water mass of the global thermohaline circulation (Orsi et al. 1999; Jacobs 2004). At the shelf break interaction between the cold mixed layer waters with the WDW produces Modified Warm Deep Water (MWDW), which is thought to be the principal water mass over the continental shelf, forming a significant proportion of the source waters for the formation of HSSW during winter (Nicholls et al. 2009). This HSSW mixes with the WDW over the shelf break to form Weddell Sea Bottom Water (WSBW) (Gill 1973; Foster and Carmack 1976), which resides in the Weddell Basin until it mixes with the overlying WSDW. As a result of the various mixing processes north of the shelf break and the conversion of MWDW to HSSW on the wide continental shelf, the FRIS in the southern Weddell Sea is well protected from the relatively warm CDW residing in the Antarctic Circumpolar Current (ACC).

In contrast, the Amundsen Sea is flooded by CDW that is only slightly modified from its source offshore in the ACC (Hellmer et al. 1998; Jacobs et al. 2011). The southern boundary of the ACC is situated just offshore of the shelf break, and seasonal wind pulses drive transport of its CDW into glacially carved troughs in the continental shelf (Walker et al. 2007; Thoma et al. 2008; Wåhlin et al. 2010). Importantly, wintertime sea ice growth does not deepen the mixed layer sufficiently to convert all of this CDW into colder shelf waters and it therefore persists at depth throughout the shelf, overlain by Winter Water (WW) formed by the remnants of winter mixed layers. The existence and variability of the warm CDW layer is thought to be implicated in the recent thinning of the ice shelves surrounding the Amundsen Sea (Shepherd et al. 2004; Pritchard et al. 2009; Jacobs et al. 2011), which are contributing increasingly to sea level rise (Meier et al. 2007).

We suppose that the temperature of the shelf seabed water masses results from a balance between the transport of warm water onto the shelf and the cooling onshelf that arises from mixed layer deepening, as shown schematically in Fig. 2. The basic geometry of the continental shelf regions is similar, so the remaining physical explanations for the observed distribution of shelf-sea temperatures can be divided into external forcings and internal feedback mechanisms. Candidate external mechanisms are (i) differing surface fluxes between the warm and cold regions, leading to a difference in sea ice production and thus the destratifying potential from brine release (Talbot 1988), and (ii) a difference in the rate and/or temperature of warm-water transport onto the shelf (Dinniman et al. 2011). Candidate internal mechanisms are (iii) warm water on-shelf reduces sea ice formation because mixed layer deepening entrains heat into the mixed layer that must be removed before further ice growth can occur (Martinson 1990); (iv) the presence of dense cold water on shelf reduces the import of less dense warm waters (Talbot 1988); and (v) warmer waters induce a greater flux of ice shelf meltwater, stratifying the water column and suppressing mixed layer deepening (Jenkins and Jacobs 2008).

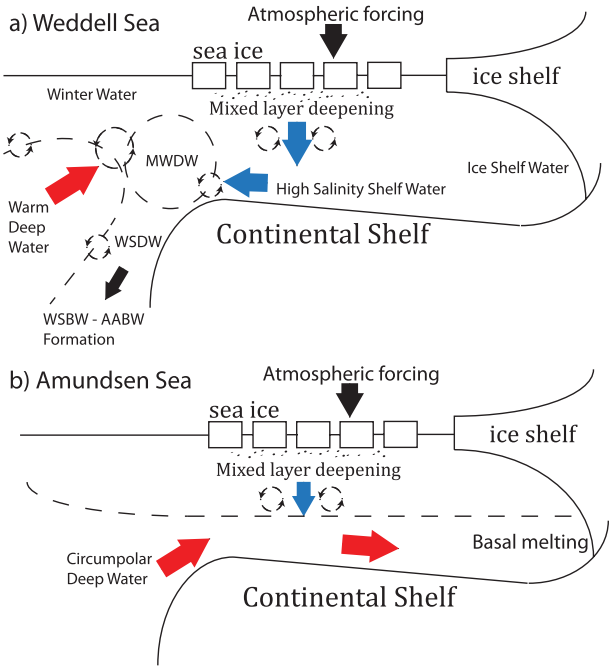

FIG. 2. Schematic of processes in the (a) Weddell and (b) Amundsen shelf seas. CDW: Circumpolar Deep Water, HSSW: high salinity shelf water, MWDW: modified warm deep water, WW: Winter Water, WSDW: Weddell Sea Deep Water, WDW: warm deep water, WSBW: Weddell Sea Bottom Water, AABW: Antarctic Bottom Water.

The principal aim of this study is to test hypothesis (i), that the bimodal distribution in continental shelf–sea temperature can be explained directly by differences in the surface fluxes (atmospheric forcing) between the two regions. A highly simplified coupled sea ice–mixed layer model is developed and applied to Amundsen and Weddell Sea test cases to study how differences in atmospheric forcing between the two regions affect the maximum wintertime mixed layer depth (MMLD). The model uses a prescribed salinity and temperature profile below the mixed layer, allowing us to assess the impact on the MMLD from changes in these shelf sea properties, testing simplistically hypothesis (ii) and (iii).

One of the first attempts to study the ocean beneath sea ice using a bulk mixed layer model was by Pollard et al. (1983), who realized the need for a more accurate representation of the oceanic heat flux into the base of the sea ice. Lemke and Manley (1984) then examined

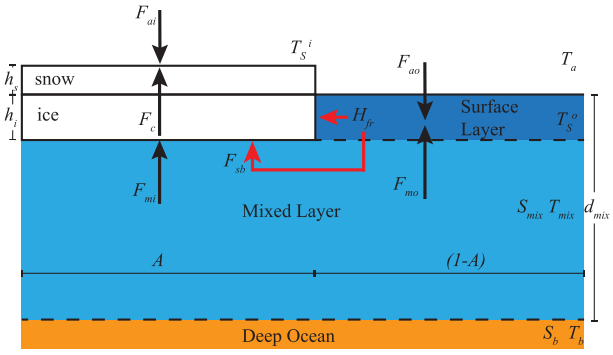

FIG. 3. Schematic diagram of the mixed layer–sea ice model and the principal thermodynamics of the sea ice growth and melt. Highlighted in red are the lateral and basal heat fluxes, calculated from the partitioning of the open water surface heat potential. F_{ao} and F_{ai} are the net incoming heat fluxes from the atmosphere over the open water and sea ice fractions, respectively.

a better representation of the pycnocline below the mixed layer, while imposing a fixed ice growth rate. Lemke (1987) included improved ice thermodynamics, while assuming that the mixed layer temperature is fixed at the freezing point, and Lemke et al. (1990) included a viscous–plastic rheology and prognostic ice concentration to study the Weddell Sea. Martinson (1990) considered winter mixed layer deepening in the Southern Ocean, assuming that wind mixing can only maintain the mixed layer depth, not change it; the mixed layer cannot store heat; double diffusion is important; the forcing is steady over the winter season; and a sharp pyncocline exists below the mixed layer. The Lemke and Martinson studies demonstrate a significant improvement in the seasonal sea ice cycle when constant deep ocean properties are replaced with more realistic ocean profiles that vary temporally and spatially. Both studies also investigated the influence of upwelling on the mixed layer. A study by Markus (1999) modeled the Southern Ocean mixed layer using a prescribed sea ice concentration from satellite data. The model applied by Tang (1991) and Tang and DeTracey (1998) to the Arctic is perhaps the closest to that presented in this paper.

The model used here builds upon these earlier studies by incorporating lateral growth of the sea ice, partitioning of the surface melt potential, an open water surface layer that transfers heat and momentum between the atmosphere and the mixed layer, and prescribed ice divergence and ambient ocean relaxation. Our main advance, however, is the detailed examination of the bimodal distribution of Antarctic shelf seas. The use of a highly simplified model provides both a complete understanding of the results and the computational simplicity necessary for the performance of a large number of sensitivity experiments. The paper is structured as follows: section 2 presents the model formulation; section 3 discusses the forcing, ocean profiles, and model parameters; section 4 presents and discusses the simulations; and concluding remarks are given in section 5.

TABLE 1. Model parameters and initial conditions used in reference simulations.

Parameter	Amundsen	Weddell
Initial mixed layer depth (m)	10	10
Initial mixed layer salinity	33.5	33.5
Initial mixed layer temp (°C)	−1.8	−1.8
Initial ice concentration	0.7	0.9
Initial ice thickness (m)	0.9	2.2
Snow thickness (m)	0.2	0.4
Divergence rate (yr^{-1})	0.4	1.0
Ocean profile	Fig. 4b	Fig. 4a
Relaxation time scale R_T (yr^{-1})	0.25	0.25
Basal melt fraction R_b	0.75	0.75

2. Model description

Our zero-dimensional coupled sea ice–ocean mixed layer model comprises four main components: (i) surface energy balances at the ice–atmosphere and ocean–atmosphere interfaces; (ii) a heat balance model describing the basal and lateral melting/freezing of the sea ice cover, which has prognostic ice thickness and concentration; (iii) an ocean mixed layer model comprising balance equations that determine the evolution of the mixed layer depth, temperature, and salinity; and (iv) an ambient ocean profile. The model components are briefly described in the following subsections and a schematic of the model is given in Fig. 3. Values for fixed parameters and constants are given in the appendix, and specific model parameters can be found in Table 1. The sea ice, open water fraction, ocean surface layer, and ocean mixed layer described in this model are illustrated schematically in Fig. 3.

a. Surface heat balance

The ice and open water surface temperatures are calculated following Maykut and Untersteiner (1971), where the snow-covered ice surface temperature T_S^i is calculated by balancing the atmospheric surface heat fluxes (sensible, latent, blackbody, incoming longwave, and incoming shortwave heat fluxes) with the conductive heat flux through the ice as

$$\rho_a c_a C_D^i U_a (T_S^i - T_a) + \rho_a L_s C_D^i U_a (q_{\text{sat}}(T_S^i) - q_a) + \epsilon_s \sigma (T_S^i)^4 - \epsilon_s F_{\text{lw}}\downarrow - (1-\alpha_s) F_{\text{sw}}\downarrow = F_c(T_S^i)\uparrow, \quad (1)$$

whereas the open water surface temperature T_S^o is calculated by balancing the atmospheric surface heat fluxes with the mixed layer to open water surface heat flux

$$\begin{aligned}&\rho_a c_a C_D^o U_a (T_S^o - T_a) + \rho_a L_v C_D^o U_a [q_{\rm sat}(T_S^o) - q_a] \\ &\quad + \epsilon_o \sigma (T_S^o)^4 - \epsilon_w F_{\rm lw}\downarrow - (1-\alpha_w)[1 - I_o(0)]F_{\rm sw}\downarrow \\ &\quad = F_{\rm mo}(T_S^o)\uparrow, \end{aligned} \tag{2}$$

where U_a is the wind speed at 10 m, $q_{\rm sat}$ is the saturation specific humidity, calculated following Taylor and Feltham (2004), q_a is the specific air humidity at 2 m, $F_{\rm lw}\downarrow$ is the incoming longwave radiative heat flux, and $F_{\rm sw}\downarrow$ is the incoming shortwave radiative heat flux.

b. Sea ice thermodynamics

We use the Semtner (1976) zero-layer sea ice model, which assumes a linear temperature gradient through the snow and sea ice, with a conductive heat flux F_c given by

$$F_c = \frac{k_i k_s (T_f - T_S^i)}{(k_i h_s + k_s h_i)}, \tag{3}$$

where h_i is the ice thickness, h_s is the thickness of the fixed snow layer, and $T_f = 273.15 - 0.054 S_{\rm mix}$ is the freezing temperature of seawater.

The heat flux into the base of the sea ice at the mixed layer–sea ice boundary $F_{\rm mi}$ is

$$F_{\rm mi} = \rho_w c_w c_h u_\star^i (T_{\rm mix} - T_f), \tag{4}$$

where $u_\star^i$ is the friction velocity between the ice and the mixed layer and $T_{\rm mix}$ is the mixed layer temperature. The heat flux from the mixed layer to the open water surface layer $F_{\rm mo}$ is

$$F_{\rm mo} = \rho_w c_w u_\star^o (T_{\rm mix} - T_S^o), \tag{5}$$

where $u_\star^o$ is the friction velocity between the open water surface layer and mixed layer.

We calculate the rate of change of ice concentration Φ_A by balancing the ocean surface heat potential, with the latent heat released/absorbed by the ice growth/melt as

$$\Phi_A = \begin{cases} \dfrac{H_{\rm fr}(1-A)}{L_f \rho_i h_i} & \text{for} \quad A < A_{\rm max} \quad \text{and} \quad T_S^o < T_f \ \text{(freezing)} \\ \dfrac{H_{\rm fr}(1-R_b)(1-A)}{L_f \rho_i h_i} & \text{for} \quad A > 0 \quad \text{and} \quad T_S^o > T_f \ \text{(melting)} \\ 0 & \text{otherwise}, \end{cases} \tag{6}$$

where A is the ice concentration and the ocean surface heat potential $H_{\rm fr}$ is calculated as

$$H_{\rm fr} = F_{\rm mo}(T_S^o) - F_{\rm mo}(T_f) = \rho_w c_w u_\star^o (T_f - T_S^o), \tag{7}$$

and $F_{\rm mo}(T_f)$ is used in the later calculation of the resultant temperature change of the mixed layer in all cases except for when $A = 0$ and $T_S^o > T_f$. Once the ice concentration grows to a maximum value ($A = A_{\rm max}$), the ocean surface heat potential is used to grow sea ice vertically. We consider this vertical growth Φ_R to actually be due to the redistribution of the sea ice grown in the persistent open water (lead) fraction, $(1 - A_{\rm max})$, by pressure ridging.

In the melting case Maykut and Perovich (1987) suggest that a considerable amount of the ocean surface heat potential can contribute to basal melting rather than lateral melting. We choose to partition the melting according to a parameter R_b, where $R_b = 0$ when all melt is lateral and $R_b = 1$ when all melt is basal, giving a basal heat flux of

$$F_{\rm sb} = \begin{cases} -H_{\rm fr} R_b (1-A) & \text{for} \quad A > 0 \quad \text{and} \quad T_S^o > T_f \\ 0 & \text{otherwise} \end{cases}. \tag{8}$$

The rate of basal melting or freezing of ice depends on the difference in heat fluxes at the mixed layer–ice interface, such that

$$\Phi_h = (F_c - F_{\rm mi} - F_{\rm sb})/(\rho_i L_f), \tag{9}$$

where a positive (negative) value of Φ_h indicates basal ice growth (melt).

Though ice dynamics are generally neglected, ice export is parameterized in this model, as it is a sink of ice concentration that can strongly affect both growth and melt phases of the sea ice annual cycle. The ice concentration sink is calculated as

$$\xi = \nabla \cdot (\mathbf{v}A), \tag{10}$$

where $\mathbf{v}$ is the sea ice velocity. Lateral gradients in ice concentration ∇A are neglected here, leaving the ice sink a function of the ice velocity divergence $A\nabla \cdot \mathbf{v}$, which is assumed to be constant and is constrained in this model by observations (Table 1).

c. Mixed layer model

The zero-dimensional mixed layer component is based on the bulk mixed layer model of Kraus and Turner (1967) and Niiler and Kraus (1977), which assumes that temperature and salinity are uniform throughout the mixed layer, and there is a full balance in the sources and sinks of turbulent kinetic energy (TKE). An integral approach can then be taken to solve the mechanical energy budget for the entire mixed layer. More sophisticated one-dimensional models have been developed since (Large et al. 1994; Price et al. 1986; Mellor and Yamada 1982), but as several of these mixing schemes have been shown to overestimate entrainment in the Weddell Sea region, (Timmermann and Beckmann 2004; Timmermann and Losch 2005), the Kraus and Turner (KT) scheme, despite also overestimating entrainment owing to its stepwise treatment of the pycnocline, is chosen for a number of reasons: (i) its simplicity means that we can completely understand the results, (ii) its computational efficiency allows us to perform large numbers of sensitivity studies, (iii) it is the simplest model able to reproduce reality, and (iv) the neglect of horizontal variations is such a large simplification that more detailed vertical treatments would represent an inconsistent level of complexity in this case.

1) Surface buoyancy fluxes

The rate of mechanical energy input to the mixed layer from surface buoyancy fluxes (power input per unit mass per unit area) is calculated as

$$P_B = c_2 d_{\text{mix}} \left(\frac{g\alpha}{\rho_w c_w} F_T\uparrow - g\beta F_S\uparrow \right), \tag{11}$$

where d_{mix} is the mixed layer depth and c_2 is a coefficient describing the power dissipation as a result of convective mixing and equals 1 (0.8) when the mixed layer is losing (gaining) energy (Tang 1991). The heat F_T and salt F_S fluxes out of the mixed layer are given by

$$F_T\uparrow = (1 - A)(F_{\text{mo}} - F^o_{\text{sw}}\downarrow) + AF_{\text{mi}}, \tag{12}$$

and

$$F_S\uparrow = \frac{\rho_i}{\rho_\omega}(S_i - S_{\text{mix}})[(\Phi_h + \Phi_R)A + \Phi_A h_i] + (P - E)S_{\text{mix}}(1 - A), \tag{13}$$

where S_{mix} is the mixed layer salinity (note that the practical salinity scale is used throughout this paper), P is the precipitation rate, and E is the evaporation rate, calculated from the latent heat flux over the open water surface. The shortwave radiation that enters the open water fraction and is absorbed within the mixed layer [longwave is assumed to be fully absorbed in the surface layer, Maykut and Untersteiner (1971)], is calculated as

$$F^o_{\text{sw}}\downarrow = F_{\text{sw}}\downarrow(1 - e^{-\kappa_w d_{\text{mix}}})(1 - \alpha_w)I_o(0). \tag{14}$$

Note that over the ice fraction, all of the incoming solar radiation is absorbed at the snow surface.

2) Wind mixing

The rate of TKE input to the mixed layer from wind stirring is calculated as

$$P_w = c_1 e^{-d_{\text{mix}}/d_w} u_\star^3, \tag{15}$$

where the effective friction velocity at the upper surface of the mixed layer $u_\star$ is calculated, assuming free drift, such that

$$u_\star = U_a \sqrt{(\rho_a/\rho_w)[AC^i_D + (1 - A)C^o_D]}. \tag{16}$$

While this assumption is prone to overestimate TKE input through wind mixing, the only alternative would be to reduce this TKE input by a certain fraction. Since the model is calibrated using several other parameters to achieve a realistic reference state, we feel a further calibration would not improve the predictive capabilities of the model.

3) Mixed layer entrainment

The power required to entrain deep water into the mixed layer at a rate w is calculated as

$$P_E = w(d_{\text{mix}}\Delta b + c_m^2), \tag{17}$$

where c_m is a bulk turbulent velocity scale representing the turbulent fluctuations of the mixed layer that will result in a frictional sink of TKE, and Δb is the difference in the buoyancy of the waters across the mixed layer base

$$\Delta b = g\alpha(T_{\text{mix}} - T_b) - g\beta(S_{\text{mix}} - S_b), \tag{18}$$

where T_b and S_b are the temperature and salinity directly below the mixed layer. This study will only consider the evolution of a stable water column where $P_E > 0$.

Balancing (11), (15), and (17) and rearranging gives the entrainment rate as

$$w = \frac{dd_{\text{mix}}}{dt} = \frac{1}{d_{\text{mix}}\Delta b + c_m^2}(P_w + P_B). \tag{19}$$

This equation is also used to reduce the depth of the mixed layer without changing the mixed layer properties, as this represents the mixed layer shallowing to a depth at which the power input from wind stirring can equal the power losses through a stabilizing surface buoyancy flux.

Conservation equations for heat and salt give the temperature and salinity evolution of the mixed layer as

$$\frac{dT_{\text{mix}}}{dt} = \begin{cases} \dfrac{-F_T\uparrow}{\rho_\omega c_w d_{\text{mix}}} + \dfrac{w}{d_{\text{mix}}}(T_b - T_{\text{mix}}) & w > 0 \\ \dfrac{-F_T\uparrow}{\rho_\omega c_w d_{\text{mix}}} & w \le 0 \end{cases} \tag{20}$$

and

$$\frac{dS_{\text{mix}}}{dt} = \begin{cases} -\dfrac{F_S\uparrow}{d_{\text{mix}}} + \dfrac{w}{d_{\text{mix}}}(S_b - S_{\text{mix}}) & \text{for} \quad w > 0 \\ -\dfrac{F_S\uparrow}{d_{\text{mix}}} & \text{for} \quad w \le 0, \end{cases} \tag{21}$$

which shows that, when we calculate a detrainment of the mixed layer, the temperature and salinity of the mixed layer can only change through surface fluxes. This is also the case when the water column is fully destratified (i.e., the mixed layer has reached the shelf seabed).

d. Ocean relaxation

The value of salinity and temperature of the ocean below the mixed layer is updated at every time step depending upon the behavior of the mixed layer. The ocean profiles are initially set to a representative summertime profile. When the mixed layer is subsequently present at any given depth, its properties are assigned to the profile at that depth. In a simplistic representation of deep ocean dynamics, wherever the mixed layer is not present the ocean profile is linearly restored toward the representative summertime profile over some time scale R_T. Remnant mixed layers can then be left behind when the mixed layer retreats back to a shallower depth, forming layers of Winter Water or dense shelf water that are slowly eroded. The representative ocean profiles are chosen to represent the water masses being transported onto the shelf in each region so as to test whether the forcings on shelf are capable of destratifying these source waters in winter.

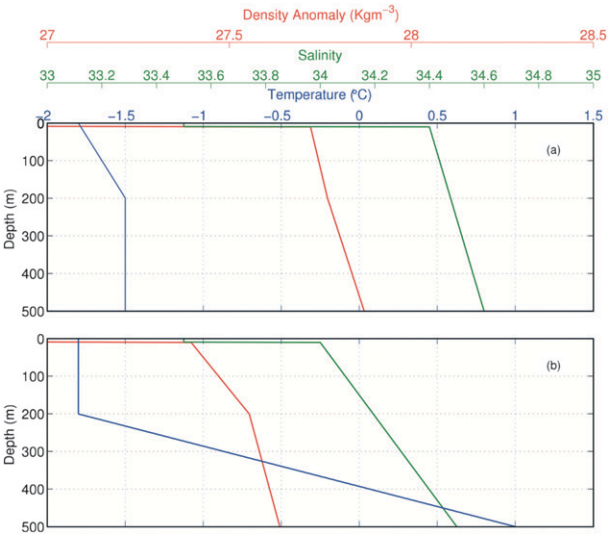

FIG. 4. Representative ocean profiles for the (a) Weddell and (b) Amundsen simulations.

3. Model setup

a. Ocean profiles

In the Weddell Sea study, we aim to model the cooling and salination of relatively warm intrusions of MWDW onto the large area of the southwestern continental shelf north of the Filchner–Ronne Ice Shelf. These intrusions appear at the middepth of the water column and have temperatures of around −1.5°C and salinities of around 34.55 (Nicholls et al. 2003, 2008). Similar intrusions are present on the continental shelf of the northwest Weddell Sea (Gordon 1998; Nicholls et al. 2004). The farthest southwest corner of the Weddell Sea features much denser HSSW with salinities as high as 34.8 (Nicholls et al. 2003), but this water is believed to be the product of the polynya at the far southern boundary of the Weddell Sea and is, therefore, not the source water mass whose modification we wish to investigate. The profile in Fig. 4a reflects the MWDW source waters and is used for all Weddell Sea simulations.

Jacobs et al. (1996) collected the first data from within the Amundsen Sea embayment, finding almost unmodified CDW right up to the ice front of Pine Island Glacier. The profiles show a distinct (~70 m) mixed layer near the freezing temperature with a salinity of ~33.8. Below the mixed layer the salinity increases

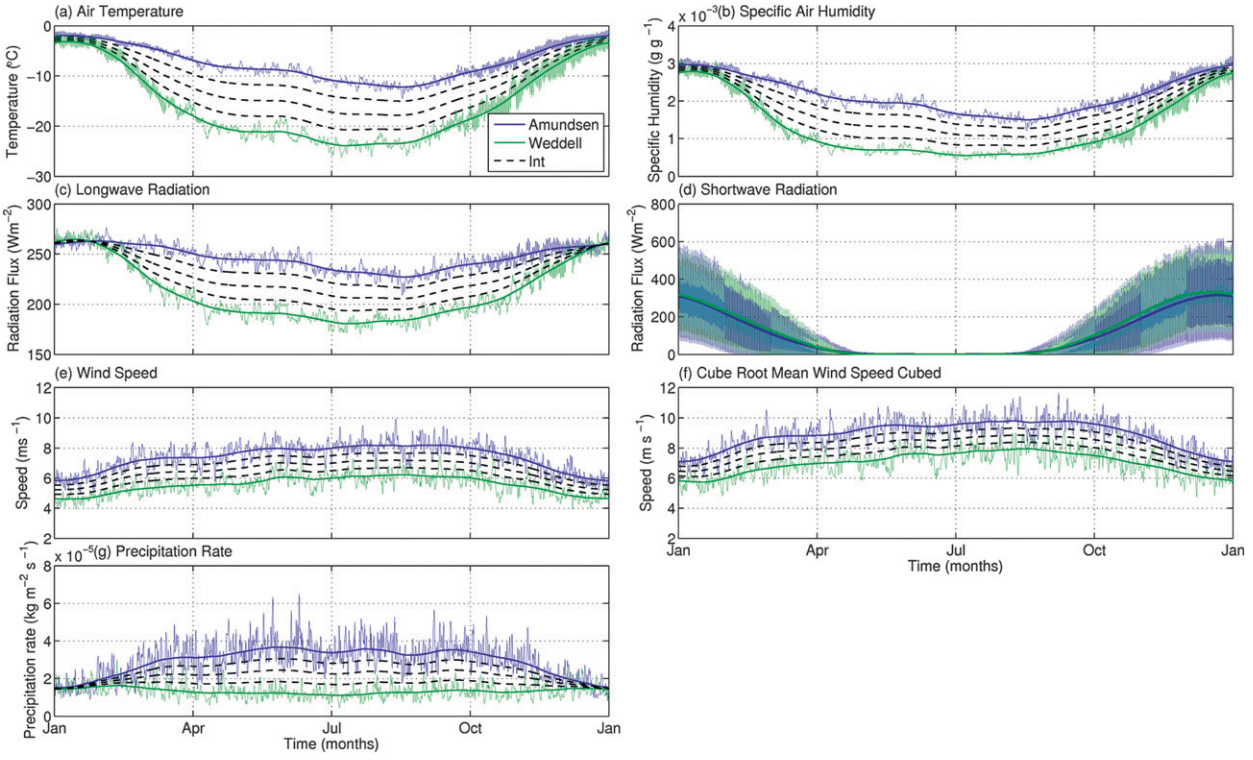

FIG. 5. Climatological forcings calculated from the NCEP–CFSv1 reanalysis data: the forcing data have been averaged spatially over each study section shown in Fig. 1 and averaged over 32 yr from 1979 to 2010. The light green (Weddell) and blue (Amundsen) lines are the raw climatologies, the thicker green and blue lines are the smoothed (30 day) forcings and the dashed black lines are the intermediate forcings used in the forcing sensitivity study.

from ~34 to ~34.5 at 600 m, while temperature increases to ~1°C; temperature and salinity are approximately constant below this. More recent data show similar profiles (Walker et al. 2007; Jacobs et al. 2011) with a deeper (~200 m) near freezing surface layer of WW north of the coast. The profile in Fig. 4b is a good fit to these data and is used for all of the Amundsen Sea simulations.

The density anomaly σ_θ is shown in Fig. 4 to illustrate the relative stability of each water column profile. The equation of state for seawater (ignoring any pressure dependence) is given by

$$\sigma_\theta(S, T, p = 0) = \rho_0[1 + \beta(S - S_0) - \alpha(T - T_0)] - 1000, \quad (22)$$

where ρ_0 is a reference density calculated from a reference salinity S_0 and temperature T_0 (UNESCO 1981).

b. *Atmospheric forcing*

The National Centers for Environmental Prediction (NCEP)–Climate Forecast System (CFS) v1 atmosphere reanalysis (Saha et al. 2006) provides us with 32 years of 6-h data (1979–2010) of air temperature (2 m), specific humidity (2 m), incoming longwave and shortwave radiation, wind speed (10 m) components, and precipitation at a resolution of 0.3125°. The forcing data for all grid points within representative areas for the Weddell and Amundsen Seas, shown in Fig. 1, were averaged over all 32 years to create climatologies, shown in Fig. 5. Note that, as the wind speed is cubed to calculate the momentum transfer into the mixed layer (15), a second wind forcing variable was created whereby the wind speed was cubed for each grid point before the spatial and temporal averaging.

There are significant differences in the climatologies of the two regions (Fig. 5), which may be summarized as (i) a similar summertime air temperature slightly below freezing (~−1°C), but a 10°C difference in the wintertime air temperature (~−23°C over the Weddell Sea and ~−13°C over the Amundsen Sea); (ii) a similar summertime humidity of ~0.003, but a 0.001 difference in the wintertime humidity (~0.0005 over the Weddell Sea and ~0.0015 over the Amundsen Sea); (iii) a similar summertime incoming longwave radiation of ~260 W m^{-2}, but a 50 W m^{-2} difference in the wintertime longwave (~180 W m^{-2} over the Weddell Sea and ~230 W m^{-2} over the Amundsen Sea); (iv) a slight seasonal cycle in the

wind speed, with an average of ~5 m s^{-1} over the Weddell Sea and ~7 m s^{-1} over the Amundsen Sea; (v) a precipitation rate that is fairly constant over the Weddell Sea, with an average value of ~1.5×10^{-5} kg m^{-2} s^{-1}, and a slight seasonal cycle over the Amundsen Sea, with an average value of ~3.1×10^{-5} kg m^{-2} s^{-1}; and (vi) no discernible difference in the incoming shortwave radiation.

From the raw climatologies, smoothed forcing datasets were created as shown by the thicker blue and green lines in Fig. 5, where a triangular smoothing procedure was used over a 30-day time period. Three intermediate forcing sets were also created for each variable (shown by the black dashed lines in Fig. 5) by linearly interpolating between the two smoothed climatologies at each time step. These intermediate forcing sets are used in a forcing sensitivity study, where each forcing is varied between the two smoothed climatologies while keeping all other forcings constant, thereby weighting each forcing change by the respective differences between each forcing variable.

c. Model parameters

Different model parameters were chosen to produce realistic reference cases for the two regions (Table 1). In particular, we sought repeating annual cycles in ice and ocean properties since these seem a logical consequence of the application of climatological fluxes. The choices are poorly constrained owing to data sparsity, so sensitivity studies were carried out to understand how each impacts the results. All simulations start on 1 January, when sea ice still covers much of the continental shelf in both the Amundsen and Weddell Seas (Comiso 2010), so a fresh initial mixed layer is combined with an initial concentration of sea ice for both studies. Ice and snow thicknesses were based on the direct observations of Worby et al. (2008), which, despite sparse data in the Amundsen Sea and the southwestern Weddell Sea in winter and studies suggesting higher precipitation in the Amundsen (e.g., van den Broeke et al. 2006), suggests thicker ice and snow in the Weddell Sea. This is clearly an area of large uncertainty but, as the snow sensitivity study demonstrates later, the results still hold for a large range of snow thicknesses. The partitioning of surface heat between lateral and basal melting is based on Steele (1992).

The ocean relaxation time scale is perhaps the least understood parameter used within the model. The relaxation is only applied to water below the mixed layer and so will only affect the remnant water masses left behind after the mixed layer has receded, meaning this parameter is more akin to a deep-water residence time. As we are relaxing to an expected summertime profile, the value is based on the time period between the mixed layer restratifying and starting to deepen again, which we take to be three months ($R_T = 0.25$) in both simulations, representing the spring season between the end of winter and the start of summer. This parameter is examined in a sensitivity study.

By multiplying the ice concentration by an ice divergence rate, we can calculate the ice export (10). Satellite-tracked ice motion vectors (Fowler 2008), for the areas shown in Fig. 1 show mean (1981–2006) annual divergence rates of 1.1 ± 0.7 yr^{-1} for the Weddell Sea and 1.0 ± 0.6 yr^{-1} the Amundsen Sea. The sensitivity studies presented later show the Amundsen to be only weakly sensitive to this parameter; however, the lower value of 0.4 yr^{-1} was used for all Amundsen studies to prevent the full removal of ice in multiyear simulations and to ensure that a repeating cycle was obtained.

The initial mixed layer depth, salinity, and temperature were based on the observed mixed layer properties at the end of preliminary simulations. All other model parameters were calibrated within the realistic ranges as discussed above to produce repeat annual cycles for the two study regions.

d. Salt and heat content of the ice–ocean column

To analyze how different processes contribute to the heat and salt content evolution of the combined sea ice, mixed layer, and deep ocean (which we will collectively refer to as the ice–ocean column in the rest of this paper), we have calculated the integral changes of heat and salt from ice export, ocean relaxation, and atmospheric surface fluxes, by integrating with respect to time over each year.

1) Annual salt content changes

The annual change in the salt content of the ice–ocean column can be a result of ice export, ocean relaxation, and precipitation minus evaporation: each are calculated respectively as

$$S_E(\mathrm{yr}) = 0.001\rho_i \int_{\mathrm{yr}-1}^{\mathrm{yr}} h_i A (S_{\mathrm{mix}} - S_i)\xi \, dt, \tag{23}$$

$$S_R(\mathrm{yr}) = 0.001\rho_i \int_{\mathrm{yr}-1}^{\mathrm{yr}} \int_{d_{\mathrm{mix}}}^{d_{\mathrm{max}}} \frac{[S_{\mathrm{init}}(z) - S(z)]\Delta z}{\tau_R} dt, \tag{24}$$

$$S_P(\mathrm{yr}) = 0.001\rho_i \int_{\mathrm{yr}-1}^{\mathrm{yr}} (E - P) S_{\mathrm{mix}} (1 - A)\, dt, \tag{25}$$

where S_{init} is the initial summertime salinity profile shown in Fig. 4 that we are relaxing the current salinity profile S toward, Δz is the ocean grid spacing and we have multiplied by $0.001\rho_i$ to express the salt content change in units of kilogram per square meter.

2) ANNUAL HEAT CONTENT CHANGES

The yearly change in the heat content of the ice–ocean column can be a result of ice export, ocean relaxation, and atmospheric surface fluxes, and each are calculated respectively as

$$H_E(\mathrm{yr}) = \int_{\mathrm{yr}-1}^{\mathrm{yr}} \rho_i L_f h_i A \xi \, dt \tag{26}$$

$$H_R(\mathrm{yr}) = \int_{\mathrm{yr}-1}^{\mathrm{yr}} \int_{d_{\mathrm{mix}}}^{d_{\max}} \frac{[T_{\mathrm{init}}(z) - T(z)] c_w \rho_w \Delta z}{\tau_R} dt, \tag{27}$$

$$H_S(\mathrm{yr}) = \int_{\mathrm{yr}-1}^{\mathrm{yr}} (1 - A)[F^o_{\mathrm{sw}}\downarrow - F_{\mathrm{mo}}(T^o_S)\uparrow] - AF_c\uparrow \, dt, \tag{28}$$

where T_{init} is the initial summertime temperature profile, shown in Fig. 4, that we are relaxing the current temperature profile T toward. Note that we are only including the export of latent heat as the zero-layer sea ice component has no capacity to store sensible heat.

4. Results and discussion

a. Amundsen and Weddell multiyear simulations

Multiyear case studies were carried out to determine how realistically the model can simulate the annual mixed layer cycle for the two different study regions, and to provide reference states for further studies. The parameters in Table 1 were chosen to produce simulations that reached a steady state (ice and ocean) after several years, as discussed in section 3c.

Within a single year, enhanced sea ice production leads to further brine rejection and thus a greater destratifying potential, resulting in a deeper MMLD in winter. Ice melt during the melt season causes the water column to restratify, with the mixed layer stabilizing and retreating back to a shallower depth. This restratification of the water column and freshening of the mixed layer is important when it comes to the following year's destratifying phase. Therefore, conditions that lead to enhanced sea ice production and thus a deeper MMLD will also provide fresher and shallower summer mixed layers if the larger storage of fresher water in the ice melts in situ in the subsequent melt season. It is therefore important to analyze the effects of perturbations over multiyear time scales to capture this complete mixed layer cycle.

Figure 6a shows a 10-yr simulation using the Weddell parameters (Table 1) and ocean profile (Fig. 4a) forced by the smoothed Weddell climatology (Fig. 5). The result is a completely destratified water column every winter (mixed layer reaching the 500 m seabed limit). The sea ice reaches a steady cycle, growing to a maximum thickness of 2.6 m and ice concentration of 0.9 in winter, and a minimum thickness of 2.2 m and ice concentration of 0.6 in summer. The mixed layer reaches a maximum salinity of 34.63, which is not quite saline enough to be classified as HSSW [typically around 34.75, Nicholls et al. (2009)]; however, this does present a realistic mechanism for converting the MWDW to near the characteristics of HSSW, with an alternative source (i.e., coastal and latent heat polynyas or shallower shelf regions) providing the final salinity increase needed.

Figure 6c shows a 10-yr simulation using Amundsen parameters (Table 1) and ocean profile (Fig. 4b) forced by the smoothed Amundsen climatology (Fig. 5). The result is a repeating MMLD of 247 m every winter. The sea ice reaches a steady state, growing to a maximum thickness of 1.1 m and ice concentration of 0.95 in winter, and a minimum thickness of 0.5 m and ice concentration of 0.5 in summer.

b. Amundsen and Weddell switched forcings simulations

As the simplest way of testing the impact of regional differences in atmospheric forcing on the mixed layer evolution, two 10-yr simulations were carried out in which the forcing sets were switched while keeping all other model conditions constant. These simulations were initiated from the steady cycles of the representative simulations described above.

Figure 6b shows a 10-yr simulation in which the Weddell reference simulation (Fig. 6a) is switched to Amundsen forcing. The result is a mixed layer that shallows and reaches a repeating MMLD of 390 m every winter. For the initial two years, the mixed layer continues to destratify the water column, during which time the sea ice undergoes rapid melting. The melting of the thicker Weddell ice freshens the mixed layer, inhibiting mixed layer deepening in the subsequent winter. By the start of the third year, the ice has melted completely and the simulation becomes ice free in all subsequent summers. As there is less ice to melt and freshen the mixed layer in later years, the mixed layer is able to deepen further until the new steady state depth is reached.

Figure 6d shows a 10-yr simulation in which the Amundsen reference simulation (Fig. 6c) is switched to Weddell forcing. The result is a mixed layer that destratifies the water column after two years of the simulation and continues to destratify every winter thereafter. The maximum ice thickness and concentration reduces in the first few years as the deep ocean heat is entrained into

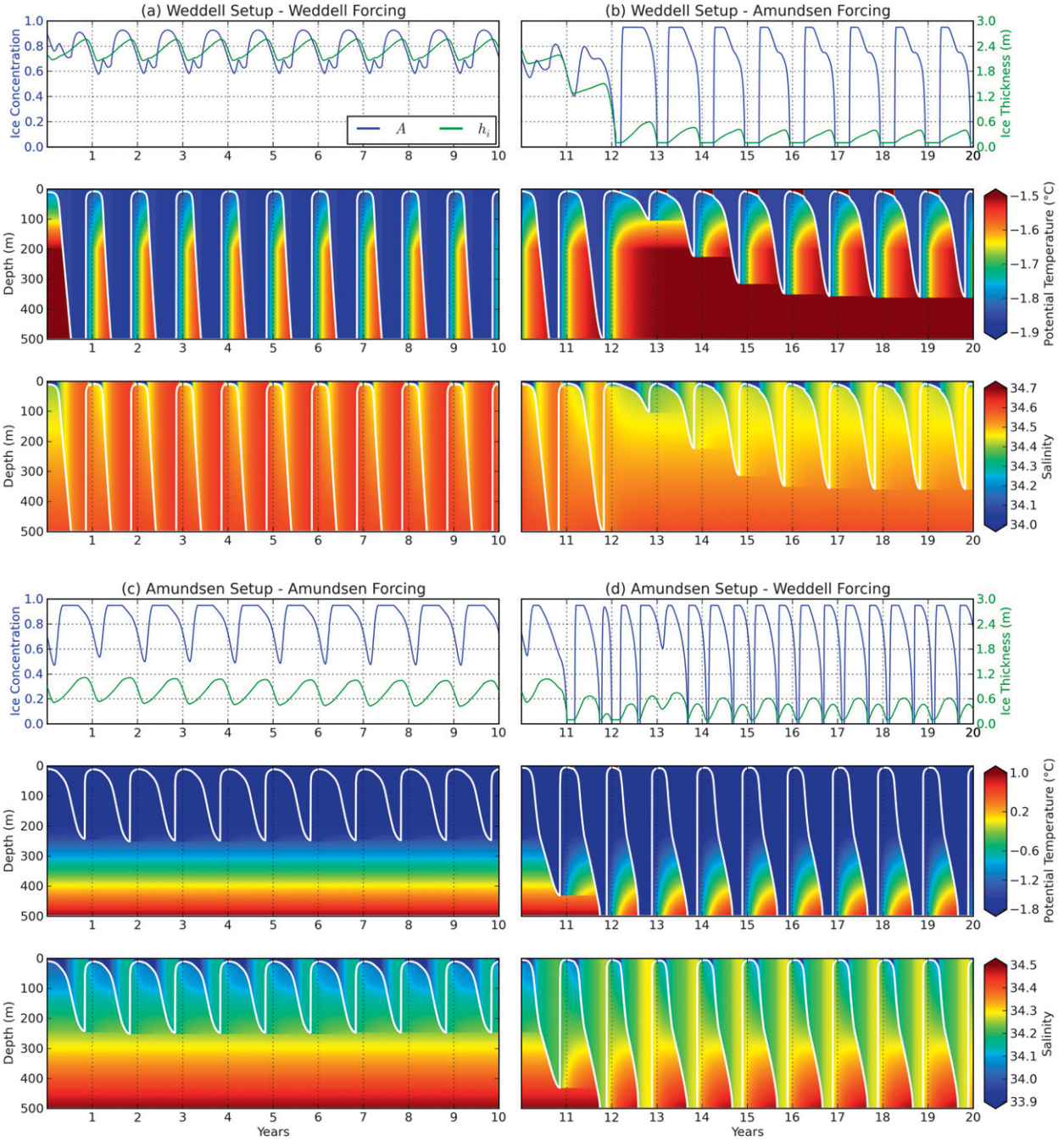

FIG. 6. Ten-year simulations using the (a) Weddell parameters, profile, and forcing; (b) applied Amundsen forcing after the Weddell spinup in (a); (c) Amundsen parameters, profile, and forcing; and (d) applied Weddell forcing after the Amundsen spinup in (c). In each subfigure the (top) ice thickness and concentration are shown with (middle) temperature and (bottom) salinity of the water column. The white line shows the mixed layer depth calculated by the model.

the mixed layer and the ice adjusts to the new ocean profile. After four years, a new ice steady state is reached in which the ice begins to grow, deepening the mixed layer, only for the ice to then melt midway through winter as the mixed layer entrains the warm Circumpolar Deep Water at depth. It is only through the mixed layer destratifying the water column midway through winter that the ice is able to grow again before the summer melt period, preventing the creation of a permanent sensible heat polynya.

This biannual ice cycle in the Amundsen setup–Weddell forcing case is clearly unrealistic. The ocean profile continues to relax toward the Amundsen ocean profile, whereas in reality a destratified water column would likely inhibit the flow of CDW onto the shelf. Nevertheless, it is interesting to note that simply switching the atmospheric forcings of the two regions appears sufficient to switch the qualitative properties of their deepest waters.

c. Salt and heat content of the ice–ocean column

To understand further the processes governing the contrasting responses discussed in the previous two sections, Fig. 7 shows the annual changes in the salt and heat content of the ice–ocean column, as discussed in section 1, with Figs. 7a–d corresponding to the simulations shown in Figs. 6a–d.

1) Salt and heat changes of the Amundsen and Weddell multiyear simulations

The annual salt and heat changes of the Weddell reference simulation in Fig. 7a show the progression toward a steady-state ocean as the net change in the annual salt and heat content tend toward zero. Initial adjustment involves a gain of salt and loss of heat that is explained by the lack of relaxation in the initial months compared with later years. For the salt content, ice export drives a large annual gain in salinity as this source of relatively fresh water leaves the system, balancing the loss of salt from a relaxation toward a fresher summertime profile as the MWDW floods back onto the shelf every year. Open ocean evaporation minus precipitation provides a negligible annual change in the salt content, which is likely due to the high ice concentration limiting the magnitude of both fluxes. For the heat content, both ice export and ocean relaxation act to increase the heat content in a similar magnitude, balancing the strong annual heat loss to the cold Weddell atmosphere.

The study by Nicholls et al. (2009) considered the formation of HSSW in the Weddell Sea and showed, using simple calculations of the expected inflow of MWDW, that the energy needed to cool and salinate these waters would require a heat loss of around 3×10^{20} J over the 370 000 km^2 continental shelf, giving a heat loss per unit area of around 8×10^8 J m^{-2}. This value lies between our calculated annual heat gain of the ice–ocean column of $\sim 6 \times 10^8$ J m^{-2} from ocean relaxation and the annual surface heat loss of $\sim 1.2 \times 10^9$ J m^{-2}.

Comparing the Amundsen reference simulation in Fig. 7c to the Weddell simulation in Fig. 7a, we see much smaller annual changes in both salt and heat content of the ice–ocean column. The contribution from ice export is reduced due to the thinner and less concentrated ice, combined with the lower ice divergence rate (0.4 s^{-1} in the Amundsen and 1.0 s^{-1} in the Weddell). The small annual change in heat from ocean relaxation is due to the shallower maximum mixed layer, with only the bottom 45 m of winter water relaxing back to a warmer temperature as we assume a 200 m cold layer of winter water to persist perennially. Salinity relaxation freshens the surface layer and salinates the water column below ~150 m, providing a negligible net change. Unlike the Weddell simulations, the small freshening from evaporation minus precipitation could be from the greater open water fraction and stronger precipitation rate.

2) Salt and heat changes of the Amundsen and Weddell switched forcings simulations

Comparing the Amundsen forced Weddell spinup simulation in Fig. 7b with the reference Weddell simulation in Fig. 7a we see a reduction in magnitude of the annual changes in the salt content from ice export and ocean relaxation and a greater loss from evaporation minus precipitation, with the annual changes in salt content evolving toward the Amundsen reference state in Fig. 7c. The annual changes in heat content reduce in magnitude in the first few years as the ice and ocean adjust to the new forcing, after which the annual heat gain from ice export reduces to near zero due to the low volume of ice persisting in the steady state, which also explains the much larger annual heat loss to the atmosphere than in the basic Amundsen case. The annual relaxation heat gain is greater in this case than in the Amundsen reference simulation as we relax a deeper mixed layer back to a profile with no thick layer of winter water.

The Weddell-forced Amundsen spinup simulation in Fig. 7d shows no discernible increase in the magnitude of the annual changes in salt content, but the annual change in heat content from ocean relaxation and atmospheric surface fluxes increase in magnitude considerably. In this simulation the mixed layer deepens and entrains the warm CDW at depth, with this heat then leaving the system through a strong atmospheric heat flux. Balancing this large loss of heat to the atmosphere is the increase in the heat content of the ice–ocean column as the thick 500-m layer of cold mixed layer waters relax to the warm Amundsen profile, creating a repeat state of heat leaving, then reentering, the ice–ocean column every year.

d. Investigating the ocean profile and atmospheric forcing

In an attempt to understand in more detail the role of both the atmospheric forcing and ocean profile in controlling the mixed layer evolution in the two regions,

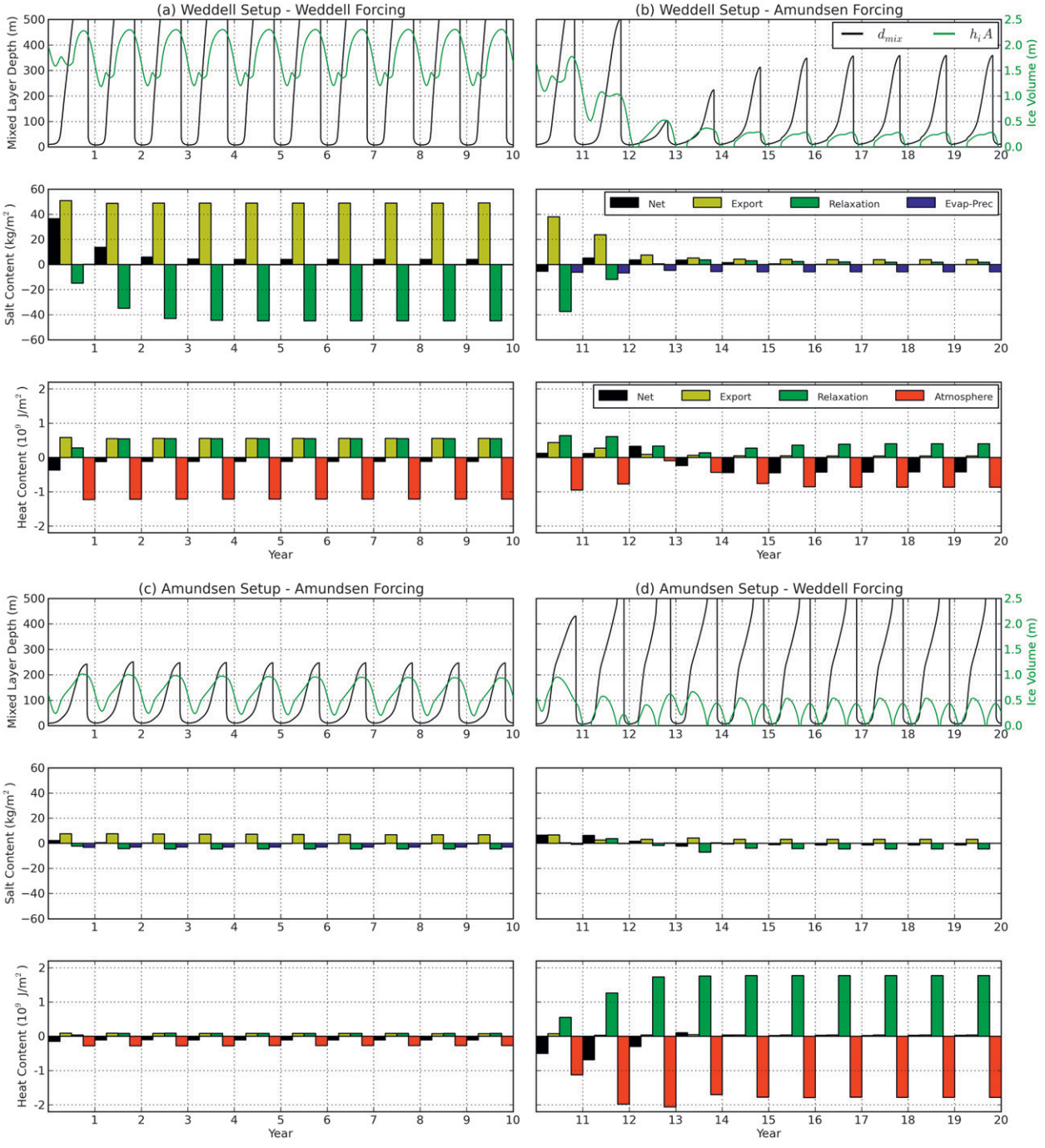

FIG. 7. Ten-year model simulations as in Figs. 6a–d: (top) the mixed layer depth and ice volume (thickness multiplied by concentration); (middle) the yearly salt content change in the ice–ocean column with contributions from ice export, ocean relaxation, and evaporation minus precipitation; and (bottom) the yearly heat content change in the ice–ocean column with contributions from ice export, ocean relaxation, and ocean–atmosphere heat flux. The net change is shown by the black bar.

Fig. 8 shows the results of the Amundsen and Weddell reference simulations with switched ocean profiles and/or the applied atmospheric forcing. Figures 8a and 8b are the reference simulations, with all other simulations showing the results of a switch after this initial spinup.

1) SWITCHING THE WEDDELL OCEAN PROFILE AND/OR FORCING

The following discussion relates to the simulations following the 10 year reference Weddell simulation in

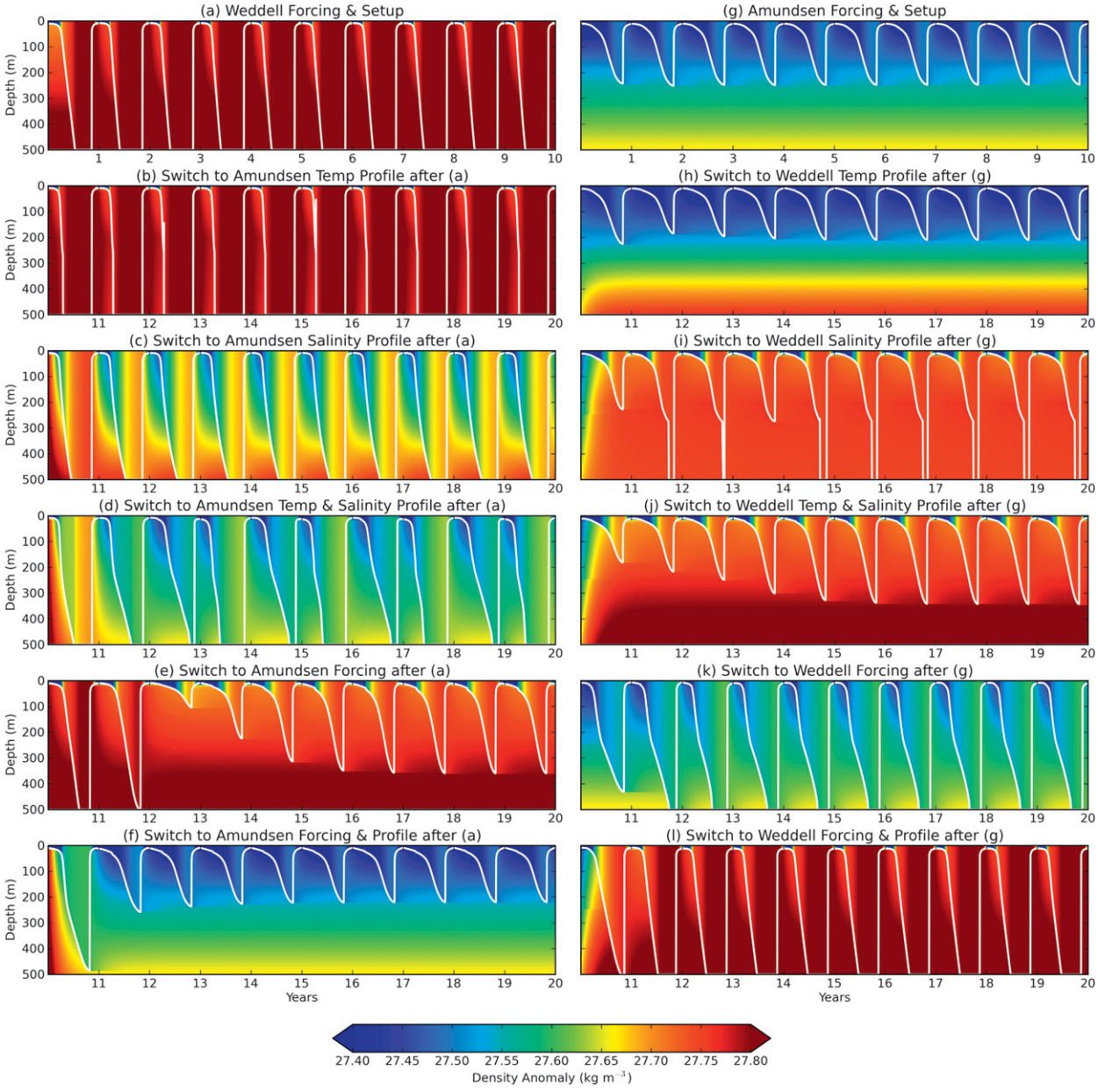

FIG. 8. Ten-year simulations for which (a) corresponds to the Weddell reference simulation in Fig. 6a and the panels below follow on from this spinup: (b) temperature profile, (c) salinity profile, (d) ocean profile, (e) atmospheric forcing, and (f) both the forcing and ocean profile have been switched to the Amundsen case. (g) Corresponds to the Amundsen reference simulation in Fig. 6c and the panels below follow on from this spin up: (h) temperature profile, (i) salinity profile, (j) ocean profile, (k) atmospheric forcing, and (l) both the forcing and ocean profile have been switched to the Weddell case.

Fig. 8a. Figure 8b shows the impact of a switch to the warmer Amundsen temperature profile.

Intuitively we may expect the inclusion of warm water at depth to slow sea ice growth and limit mixed layer deepening, but the switch to the warmer and lower density temperature profile has reduced the stability of the profile at depth. So, the mixed layer entrains rapidly after a depth of around 250 m because the mixed layer density matches that of the constant density profile below. In this specific case, ocean heat can therefore enhance mixed layer deepening while slowing sea ice growth.

Figure 8c shows the impact of a switch to the fresher and more stratified Amundsen salinity profile. Despite the more stable profile, which implies that a larger mixed layer density cycle is required to destratify the water

column every year, the mixed layer still deepens to the seabed at around the same time as in the reference Weddell simulation. However, by entraining into a fresher profile, the maximum mixed layer salinity (MMLS) is less than in the reference case.

Figure 8d shows the impact of a switch to both the Amundsen salinity and temperature profile. This profile is stable, preventing the inclusion of warm water from causing rapid deepening. The system evolves into a 2-yr cycle in which the sea ice is removed fully in winter through melting and ice export, with the mixed layer still deepening and salinating from the large destabilizing surface temperature flux driving mixed layer entrainment. The lack of a fresh summertime profile then allows for rapid mixed layer deepening in the following year, removing all of the deep ocean heat before the end of winter, allowing the ice to grow again. This then melts in the following summer, freshening the mixed layer, and the cycle begins again.

Figure 8e shows the impact of a switch to the Amundsen forcing only and is the same as Figs. 6b and 7b so will not be discussed further.

Figure 8f shows the impact of a switch to both the Amundsen ocean profile (temperature and salinity) and forcing. Within one year of the simulation the system has evolved to a similar state to the reference Amundsen simulation in Fig. 8g, with the mixed layer reaching a depth of 220 m every winter. The difference of 25 m in the maximum mixed layer depth could be from differences in the model setups. The increased ice divergence rate in the Weddell can increase the open water fraction in summer, increasing the potential for summertime melting and freshening of the mixed layer. Also the thicker snow cover (0.4 m in the Weddell simulations compared to 0.2 m in the Amundsen simulations) will reduce the surface heat fluxes, limiting sea ice growth and the resultant mixed layer deepening. This is investigated further in the model parameter sensitivity studies shown later.

2) Switching the Amundsen ocean profile and/or forcing

The following discussion relates to the simulations following the 10-yr reference Amundsen simulation in Fig. 8g.

Figure 8h shows the impact of a switch to the colder Weddell temperature profile. Despite the Weddell profile being colder at depth, it is warmer above 200 m, which is more important in the Amundsen as only the top 200–300 m of the ocean is entrained. This warmer summertime surface layer limits sea ice growth and the resultant mixed layer deepening. The result is a repeating MMLD of 210 m.

Figure 8i shows the impact of a switch to the denser but less stratified Weddell salinity profile. Similar to Fig. 8c, the water column is now relaxing to a near constant density profile, with rapid entrainment taking place at around 250 m when the mixed layer density matches that of the constant profile below. The mixed layer increases faster than in the reference Amundsen simulation because the fresh winter water layer has been replaced with relatively saline waters below the summertime mixed layer. Relaxing to an unstable profile is unrealistic, but it does highlight the importance in the Amundsen case of a well-stratified salinity profile in maintaining a shallow mixed layer.

Figure 8j shows the impact of a switch to both Weddell salinity and temperature profiles. This combination is stable, unlike the switch to just the Weddell salinity profile, and as a result there is no rapid deepening. The result is an evolution toward a new steady-state MMLD of 340 m. This demonstrates that the Weddell salinity profile, despite being more saline, is less stratified and thus allows for deeper mixed layers, as the mixed layer increases its salinity faster by entraining this higher salinity water earlier in the year.

Figure 8k shows the impact of a switch to the Weddell forcing and is the same as Figs. 6d and 7d, so will not be discussed further.

Figure 8l shows the impact of a switch to the Weddell ocean profile (temperature and salinity) and forcing. The mixed layer reaches the seabed in all winters, creating a similar ocean profile evolution to the reference Weddell simulation. The thinner snow cover and reduced divergence rate cause an annual increase in the ice volume, which does not appear to prevent the mixed layer from reaching the seabed every winter.

e. Sensitivity to changes in the atmospheric forcing

To understand the role played by each of the separate atmospheric forcing variables, a forcing sensitivity study was carried out as shown in Fig. 9. Each forcing is incremented in turn between the two forcing sets, as shown in Fig. 5, starting at the beginning of the two reference simulations. The MMLD is used as the diagnostic in both cases; however, as the Weddell mixed layer reaches the seabed in virtually all cases, the MMLS is also used as a diagnostic for the Weddell study as it quantifies the duration and strength of the destratification phase and is of practical interest in the formation of dense shelf waters and ultimately AABW. Figure 9 shows the results after 1, 5, and 10 years to demonstrate the evolution of the mixed layer under each forcing change.

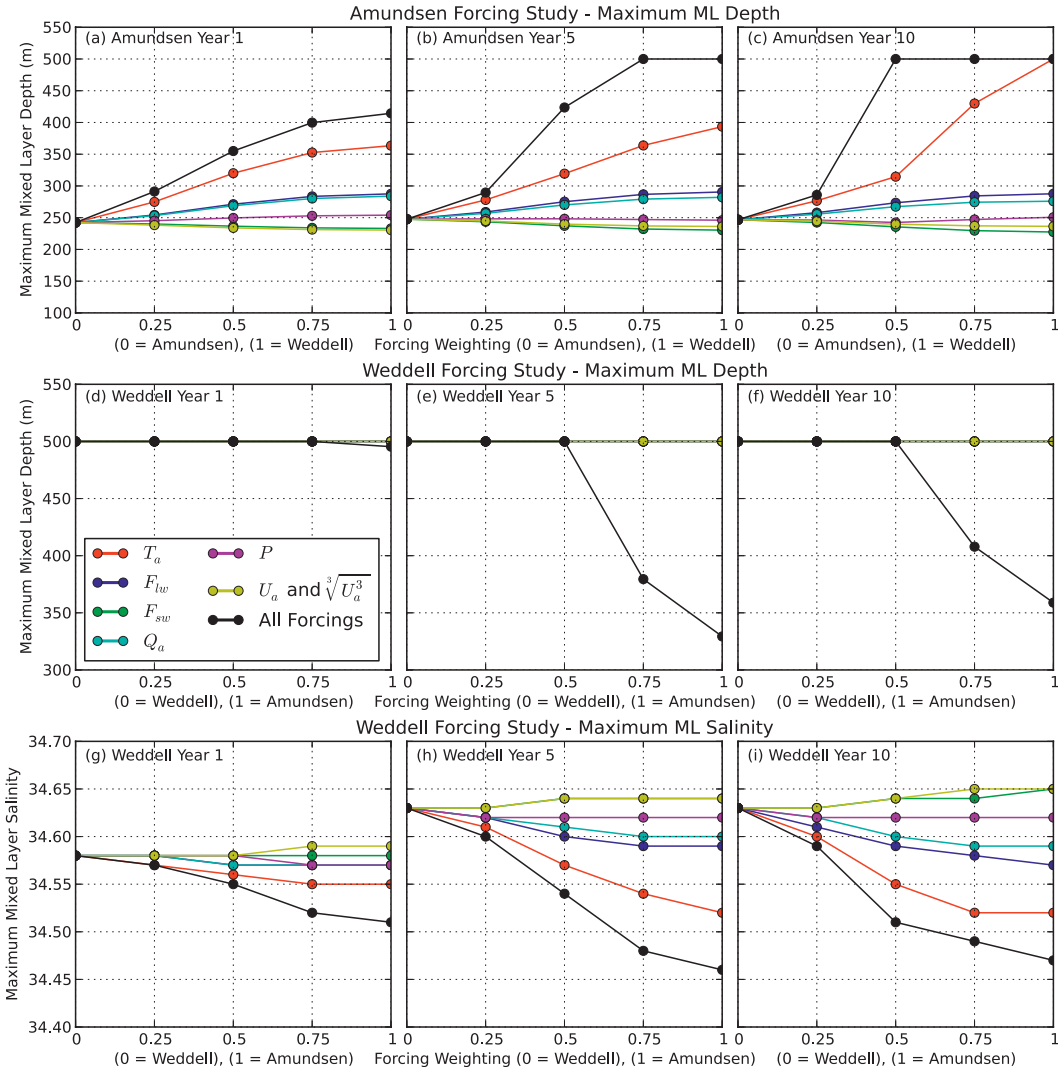

FIG. 9. Forcing sensitivity study for both the Weddell and Amundsen simulations. (a)–(c) The Amundsen maximum mixed layer depth sensitivities after 1, 5, and 10 years where the forcing for each variable (shown in the legend) is incremented toward the Weddell forcing, using the intermediate forcings shown in Fig. 5, and (d)–(f) the Weddell maximum mixed layer depth sensitivities after 1, 5, and 10 years. The results of all the individual forcing maximum mixed layer depth sensitivities are equal to 500 m. (g)–(i) The Weddell maximum mixed layer salinity sensitivities after 1, 5, and 10 years.

1) AMUNDSEN FORCING STUDY

Figures 9a–c show the response of the Amundsen MMLD to changes in each forcing. The impacts of a switch in the precipitation, incoming longwave and shortwave radiation, air humidity, and wind speed after 1, 5, and 10 years have similar magnitudes. The change in precipitation has no discernible impact on the MMLD (reference Amundsen MMLD = 247 m); switching the incoming shortwave radiation (227 m, year 10) and wind speed (236 m, year 10) switch act to reduce the MMLD slightly; switching the incoming longwave (288 m, year 10) and humidity (276 m, year 10) increases the MMLD slightly. Switching the air temperature has the biggest impact, increasing the MMLD to 363 m in the first year and causing a complete destratification (MMLD = 500 m) after 10 years. Switching all the forcings has a greater impact still, destratifying the water column after 5 years with a 0.75 weighted switch and after 10 years with only a 0.50 weighted switch.

2) WEDDELL FORCING STUDY

Figures 9d–f show the response of the Weddell MMLD to changes in each forcing. Only through switching all the forcing variables together can we prevent the mixed layer

from destratifying the water column. It may also be true that a combination of specific forcings could also prevent destratification; however, this was not investigated as it would have involved a considerably greater number of simulations.

Figures 9g–i show the response of the Weddell MMLS. In this plot a higher salinity indicates a mixed layer that has more destratifying potential, where either the rate or period of destratification is increased. It is expected that, were the seabed deeper than 500 m, the results with the highest MMLS would be more likely to destratify the deeper water column. The order of sensitivity to the different forcings is similar to the Amundsen case, but the reference salinity increases from year 1 to year 5 before stabilizing, and the sensitivity to each forcing appears to increase from year 1 through to 10. The precipitation rate switch shows no discernible impact, the incoming shortwave (34.65, year 10) and wind speed (34.65, year 10) switch increase the MMLS slightly (reference Weddell MMLS of 34.63), the humidity (34.59, year 10) and incoming longwave (34.57, year 10) switch decrease the MMLS, and air temperature has the greatest impact, reducing the MMLS to 34.52 in year 10.

f. Sensitivity to model parameters

Several model parameter sensitivity studies were carried out, including the impact of the initial mixed layer depth, salinity, and temperature, and initial ice thickness and concentration on the MMLD. As these initial condition sensitivity tests showed no impact on the long-term (year 10) repeating solutions, the results are not shown. Instead, the impact of the partitioning of surface heat between lateral and basal melt, the ocean relaxation time period, the ice divergence rate, and the snow thickness are all shown in Fig. 10. In a similar fashion to the forcing sensitivity study, changes in these model parameters did not prevent the Weddell mixed layer from destratifying the water column, so the MMLS was used to quantify the impact in the Weddell simulation. The following sensitivity studies discuss the results of a change in each parameter from the values used in both reference simulations. In some cases the range shown is greater than the range discussed to demonstrate the impact of both a decrease and increase in the given parameter.

1) SENSITIVITY TO THE PARTITIONING OF SURFACE HEAT R_b

Figure 10a shows the sensitivity of the MMLD to the partitioning of the open-ocean surface heat potential between lateral and basal melting. Using all of the surface heat to melt laterally (decreasing R_b from 0.75 to 0) in the Amundsen study results in a slight decrease in the MMLD from 247 m to 220 m. In contrast, the Weddell this results in an increase in the MMLS from 34.63 to 34.77.

In the Amundsen, greater lateral melting opens up more open water, which is then exposed to the warm atmosphere in the summer melt season, causing more melting. In the Weddell, minimizing the ice concentration by combining the use of all the surface heat for lateral melting with the strong Weddell ice divergence rate will maximize the potential heat loss to the cold Weddell atmosphere, enhancing the destratifying potential.

2) SENSITIVITY TO THE OCEAN RELAXATION TIME SCALE R_T

Figure 10b shows the sensitivity of the MMLD to the ocean relaxation time scale. Increasing this by a factor of 4 (increasing R_T from 0.25 yr^{-1} to 1 yr^{-1}), and thus decreasing the strength of the ocean relaxation causes an increase in the Amundsen MMLD from 247 to 275 m and an increase in the Weddell MMLS from 34.63 to 34.70.

A higher relaxation time scale is analogous to a slower rate of warmer summertime waters flowing back onto the shelf, and the slower erosion of the cold winter water. Bringing less heat onto the shelf thus reduces the ocean heat flux that could inhibit sea ice growth and mixed layer deepening. It also prevents the salinity restratification that can also slow mixed layer deepening in subsequent years.

3) SENSITIVITY TO THE ICE DIVERGENCE RATE ξ

Figure 10c shows the sensitivity of the MMLD to the ice divergence rate. Both cases show a weak, nonmonotonic response of the MMLD to this parameter. In the Amundsen case a decrease in the divergence rate from 0.4 to 0.1 s^{-1} increases the MMLD from 247 to 263 m. Increasing the divergence rate to 0.7 s^{-1} results in the minimum MMLD of 233 m, with an increase to the Weddell divergence rate of 1.0 s^{-1} increasing the MMLD to 255 m. In the Weddell case a decrease in the divergence rate from 1.0 to 0.4 s^{-1} reduces the MMLS from 34.63 to 34.59, while an increase in the divergence rate to 1.3 s^{-1} also reduces the MMLS from 34.63 to 32.62.

Sea ice export is an important mechanism for creating open water, which has a strong seasonal impact on the mixed layer evolution. In winter, ice divergence acts to increase sea ice production as the open water fraction increases, through which heat is able to escape more efficiently. In summer, an increased open water fraction increases the atmosphere to surface heat flux, increasing sea ice melt and solar heating of the mixed layer. Increased sea ice growth leads to deeper mixed layers, whereas the increased melting and warming stabilizes the

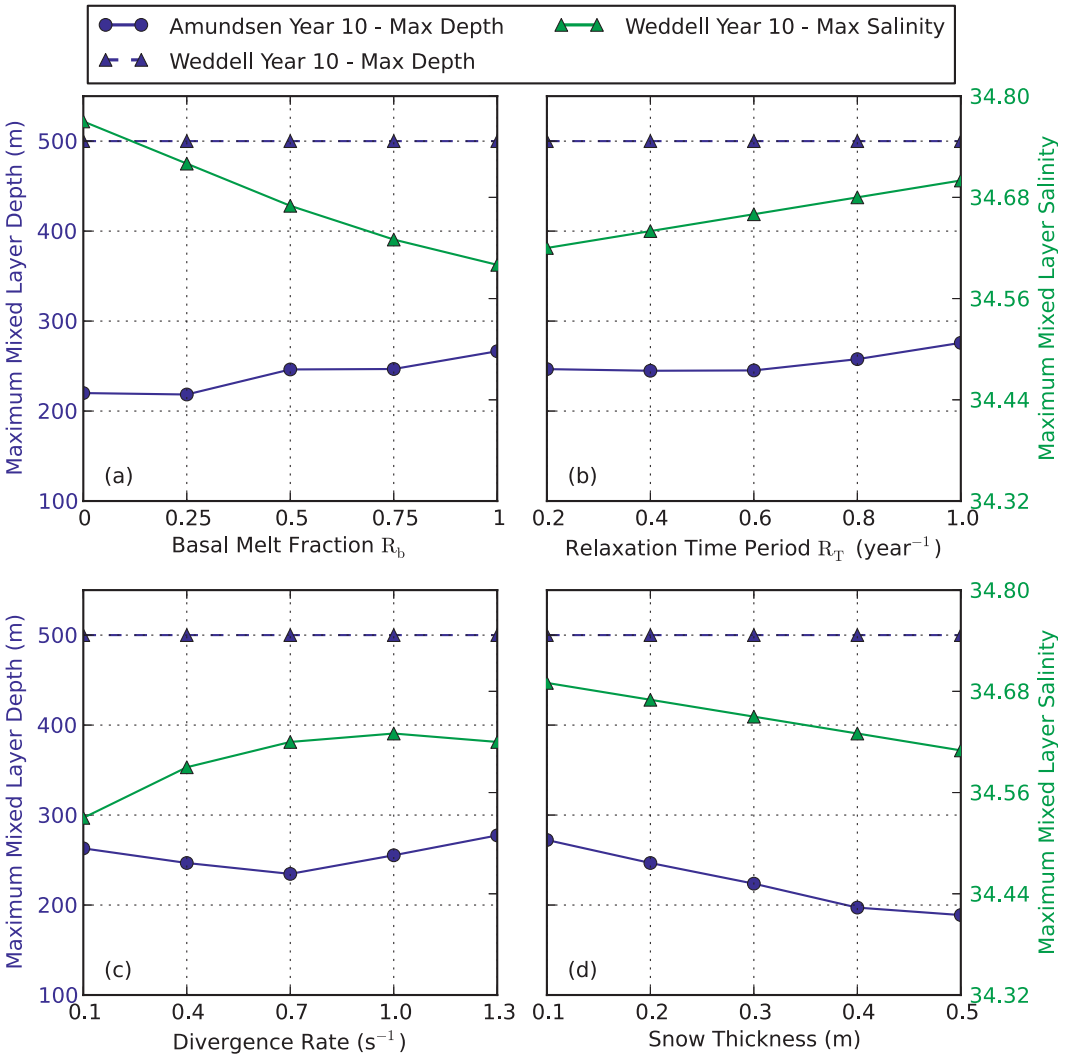

FIG. 10. Sensitivity study of model parameters for both the Weddell and Amundsen model setups starting from the reference simulations in Figs. 6a and 6c. The blue lines show the sensitivity of the maximum mixed layer depth to each parameter for both the Amundsen (solid/circles) and Weddell (dashed/triangles), while the green line shows the sensitivity of the maximum mixed layer salinity for the Weddell study only.

mixed layer, inhibiting the mixed layer deepening of the following year. While it is expected that very high divergence rates (i.e., those expected in a latent heat polynya) lead to deeper mixed layers, this sensitivity study shows that small increases can have the opposite effect.

4) SENSITIVITY TO THE CONSTANT SNOW THICKNESS H_S

Figure 10e shows the sensitivity of the MMLD to the constant snow thickness. An increase in the snow thickness in the Amundsen study from 20 cm to the Weddell thickness of 40 cm decreases the MMLD from 247 to 200 m. The respective decrease in the Weddell to the Amundsen snow thickness increases the MMLS from 34.63 to 34.67.

In winter, snow prevents the rapid growth of sea ice, with the low thermal conductivity of snow insulating the ocean from the atmosphere. During the melt season, the snow cover reduces the rate of sea ice melt. This sensitivity shows that it is the impact on the ice growth that is the dominant factor.

5. Conclusions

A coupled sea ice–mixed layer model has been used to investigate the physical processes underlying the bimodal distribution in water mass temperature over the Antarctic continental shelf. The model is able to successfully simulate realistic sea ice and mixed layer annual cycles, with complete destratification of the Weddell Sea

and only partial destratification of the Amundsen Sea. Multiyear simulations indicate the need to include realistic regional surface fluxes, relaxation to representative ocean profiles, and tuned ocean/ice parameters to produce a mixed layer annual cycle that is representative of the two study regions. The Weddell Sea simulations show a large annual loss of salt from the relaxation to a fresher modified warm deep water profile in summer, which is balanced by an annual gain in salt from the export of relatively fresh ice. The large annual loss of heat to the atmosphere is balanced equally by the heat gain from ice export and ocean relaxation. The magnitude of the annual salt and heat changes are considerably lower in the Amundsen Sea simulations.

The multiyear simulations also show a complete destratification of the Amundsen Sea by the application of Weddell Sea forcings, while the Amundsen-forced Weddell Sea simulations reach a new equilibrium maximum mixed layer depth in winter that is shallower than the shelf seabed. In all cases, the atmospheric forcing plays the primary role in determining whether the mixed layer destratifies the water column, though the ocean profile is shown to play a secondary role in determining the maximum salinity of the destratified water column and the maximum depths of the shallower mixed layers. Only by combining a switch in forcing and ocean profile are we able to realistically switch from one reference state to the other.

The model prediction of maximum mixed layer depth is most sensitive to air temperature differences between the two study regions, but differences in the incoming longwave radiation and air humidity are also important, with the difference in wind speed, precipitation and incoming shortwave radiation only providing a weak response. In the Weddell, only through switching all forcing variables to the Amundsen forcing are we able to prevent the complete destratification of the water column.

Our simple model cannot conclude that any single mechanism controls the observed bimodal distribution in the shelf water-mass temperature. Nevertheless, the study builds understanding of the many feedbacks involved, and the switched forcing results lend strong support to the hypothesis of Talbot (1988) that differences in atmospheric forcings are sufficient to explain the difference in water mass temperature over the Antarctic continental shelf.

APPENDIX

Notation

a. Constants

α thermal expansion coefficient, 5.82×10^{-5} K^{-1}
β saline contraction coefficient, 8×10^{-4}
c_a specific heat capacity of air, 1005 J kg^{-1} K^{-1}
c_w specific heat capacity of water, 4190 J kg^{-1} K^{-1}
ϵ_s longwave emissivity of snow, 1
ϵ_w longwave emissivity of open water, 0.97
G acceleration due to gravity, 9.81 m s^{-2}
k_i thermal conductivity of ice, 2.04 W m^{-1} K^{-1}
k_s thermal conductivity of snow, 0.31 W m^{-1} K^{-1}
L_f latent heat of fusion, 3.340×10^5 J kg^{-1}
L_s latent heat of sublimation, 2.834×10^6 J kg^{-1}
L_v latent heat of vaporisation, 2.501×10^6 J kg^{-1}
p_{atm} atmospheric pressure, 100 kPa
ρ_w density of water, 1026 kg m^{-3}
ρ_i density of ice, 930 kg m^{-3}
ρ_a density of air, 1.275 kg m^{-3}
σ Stefan-Boltzmann constant, 5.67×10^{-8} W m^{-2} K^{-4}

b. Fixed parameters

$A_{\max}$ prescribed maximum ice concentration, 0.95
α_s albedo of snow, 0.8
α_w albedo of water, 0.06
c_1 maximum magnitude of wind stirring in the mixed layer, 0.8 (Tang 1991)
C_D^i turbulent transfer coefficient over ice fraction, 0.0013 (Ebert and Curry 1993)
C_D^o turbulent transfer coefficient over lead fraction, 0.001 (Ebert and Curry 1993)
c_h Stanton number for mixed layer to sea ice heat transfer, 0.006 (McPhee 1992)
c_m unsteadiness coefficient, 0.03 m s^{-1} (Kim 1976)
d_w scale depth of dissipation, 10 m (Lemke and Manley 1984)
$h_{\min}$ minimum sea ice thickness, 0.1 m
$I_o(0)$ fraction of shortwave radiation that penetrates the open water surface layer, 0.45 (Niiler and Kraus 1977)
κ_w extinction coefficient of shortwave solar radiation in ocean waters, 0.1 m^{-1} (Kara et al. 2005)
S_i average bulk salinity of sea ice, 5
Δz ocean profile vertical resolution, 0.5 m

REFERENCES

Comiso, J., 2010: *Polar Oceans from Space*. Springer, 507 pp.

Dinniman, M. S., J. M. Klinck, and W. O. Smith Jr., 2011: A model study of Circumpolar Deep Water on the West Antarctic Peninsula and Ross Sea continental shelves. *Deep-Sea Res. II,* **58,** 1508–1523, doi:10.1016/j.dsr2.2010.11.013.

Ebert, E. E., and J. A. Curry, 1993: An intermediate one-dimensional thermodynamic sea ice model for investigating ice-atmosphere interactions. *J. Geophys. Res.,* **98** (C6), 10 085–10 109.

Fahrbach, E., G. Rohardt, M. Schröder, and V. Strass, 1994: Transport and structure of the Weddell Gyre. *Ann. Geophys.,* **12,** 840–855, doi:10.1007/s00585-994-0840-7.

Foldvik, A., T. Gammelsrd, and T. Trresen, 1985: Hydrographic observations from the Weddell Sea during the Norwegian Antarctic research expedition 1976/77. *Polar Res.,* **3,** 177–193, doi:10.1111/j.1751-8369.1985.tb00506.x.

——, and Coauthors, 2004: Ice shelf water overflow and bottom water formation in the southern Weddell Sea. *J. Geophys. Res.,* **109,** C02015, doi:10.1029/2003JC002008.

Foster, T. D., and E. C. Carmack, 1976: Frontal zone mixing and antarctic bottom water formation in the southern Weddell Sea. *Deep-Sea Res. Oceanogr. Abstr.,* **23**, 301–317.

Fowler, C., cited 2008: Polar pathfinder daily 25 km EASE-grid sea ice motion vectors, [1981–2006]. National Snow and Ice Data Center, Boulder, CO, digital media. [Available online at http://nsidc.org/data/docs/daac/nsidc0116_icemotion.gd.html.]

Gill, A. E., 1973: Circulation and bottom water production in the Weddell Sea. *Deep-Sea Res. Oceanogr. Abstr.,* **20,** 111–140.

Gordon, A. L., 1998: *Western Weddell Sea Thermohaline Stratification.* Antarctic Research Series, Vol. 75, Amer. Geophys. Union, 215–240.

——, B. Huber, D. McKee, and M. Visbeck, 2010: A seasonal cycle in the export of bottom water from the Weddell Sea. *Nat. Geosci.,* **3,** 551–556.

Gouretski, V., and K. P. Koltermann, 2004: WOCE Global Hydrographic Climatology. *Ber. Bundesamtes Seeschifffahrt Hydrogr. Tech.,* **35,** 1–52.

Hellmer, H. H., S. S. Jacobs, and A. Jenkins, 1998: Oceanic erosion of a floating Antarctic glacier in the Amundsen Sea. *Ocean, Ice, and Atmosphere: Interactions at the Antarctic Continental Margin,* Antarctic Research Series, Vol. 75, 83–99.

Jacobs, S. S., 2004: Bottom water production and its links with the thermohaline circulation. *Antarct. Sci.,* **16,** 427–437, doi:10.1017/S095410200400224X.

——, A. F. Amos, and P. M. Bruchhausen, 1970: Ross Sea oceanography and Antarctic Bottom Water formation. *Deep-Sea Res. Oceanogr. Abstr.,* **17,** 935–962.

——, H. H. Hellmer, and A. Jenkins, 1996: Antarctic ice sheet melting in the Southeast Pacific. *Geophys. Res. Lett.,* **23,** 957–960.

——, A. Jenkins, C. F. Giulivi, and P. Dutrieux, 2011: Stronger ocean circulation and increased melting under Pine Island Glacier ice shelf. *Nat. Geosci.,* **4,** 519–523, doi:10.1038/ngeo1188.

Jenkins, A., and S. Jacobs, 2008: Circulation and melting beneath george vi ice shelf, Antarctica. *J. Geophys. Res.,* **113,** C04013, doi:10.1029/2007JC004449.

Kara, A. B., A. J. Wallcraft, and H. E. Hurlburt, 2005: A new solar radiation penetration scheme for use in ocean mixed layer studies: An application to the Black Sea using a fine-resolution hybrid coordinate ocean model (HYCOM). *J. Phys. Oceanogr.,* **35,** 13–32.

Kim, J.-W., 1976: A generalized bulk model of the oceanic mixed layer. *J. Phys. Oceanogr.,* **6,** 686–695.

Kraus, E. B., and J. S. Turner, 1967: A one-dimensional model of the seasonal thermocline II. The general theory and its consequences. *Tellus,* **19,** 98–106, doi:10.1111/j.2153-3490.1967.tb01462.x.

Large, W. G., J. C. McWilliams, and S. C. Doney, 1994: Oceanic vertical mixing: A review and a model with a nonlocal boundary layer parameterization. *Rev. Geophys.,* **32,** 363–403, doi:10.1029/94RG01872.

Lemke, P., 1987: A coupled one-dimensional sea ice-ocean model. *J. Geophys. Res.,* **92** (C12), 13 164–13 172.

——, and T. O. Manley, 1984: The seasonal variation of the mixed layer and the pycnocline under polar sea ice. *J. Geophys. Res.,* **89** (C4), 6494–6504.

——, W. B. Owens, and W. D. Hibler, 1990: A coupled sea ice-mixed layer-pycnocline model for the Weddell Sea. *J. Geophys. Res.,* **95** (C6), 9513–9525.

Markus, T., 1999: Results from an ECMWF–SSM/I forced mixed layer model of the Southern Ocean. *J. Geophys. Res.,* **104** (C7), 15 603–15 620.

Martinson, D. G., 1990: Evolution of the Southern Ocean winter mixed layer and sea ice: Open ocean deepwater formation and ventilation. *J. Geophys. Res.,* **95** (C7), 11 641–11 654.

——, S. Stammerjohn, R. Smith, and R. Iannuzzi, 2008: Palmer, Antarctica, long-term ecological research program first 12 years: Physical oceanography, spatio-temporal variability. *Deep-Sea Res. II,* **55,** 1964–1987, doi:10.1016/j.dsr2.2008.04.038.

Maykut, G. A., and N. Untersteiner, 1971: Some results from a time-dependent thermodynamic model of sea ice. *J. Geophys. Res.,* **76,** 1550–1575.

——, and D. K. Perovich, 1987: The role of shortwave radiation in the summer decay of a sea ice cover. *J. Geophys. Res.,* **92** (C7), 7032–7044.

McPhee, M. G., 1992: Turbulent heat flux in the upper ocean under sea ice. *J. Geophys. Res.,* **97** (C4), 5365–5379.

Meier, M. F., M. B. Dyurgerov, U. K. Rick, S. O'Neel, W. T. Pfeffer, R. S. Anderson, S. P. Anderson, and A. F. Glazovsky, 2007: Glaciers dominate eustatic sea-level rise in the 21st century. *Science,* **317,** 1064–1067.

Mellor, G. L., and T. Yamada, 1982: Development of a turbulence closure model for geophysical fluid problems. *Rev. Geophys.,* **20,** 851–875.

Nicholls, K. W., L. Padman, M. Schröder, R. A. Woodgate, A. Jenkins, and S. Østerhus, 2003: Water mass modification over the continental shelf north of Ronne Ice Shelf, Antarctica. *J. Geophys. Res.,* **108,** 3260, doi:10.1029/2002JC001713.

——, C. J. Pudsey, and P. Morris, 2004: Summertime water masses off the northern Larsen C Ice Shelf, Antarctica. *Geophys. Res. Lett.,* **31,** L09309, doi:10.1029/2004GL019924.

——, L. Boehme, M. Biuw, and M. A. Fedak, 2008: Wintertime ocean conditions over the southern Weddell Sea continental shelf, Antarctica. *Geophys. Res. Lett.,* **35,** L21605, doi:10.1029/2008GL035742.

——, S. Østerhus, K. Makinson, T. Gammelsrød, and E. Fahrbach, 2009: Ice-ocean processes over the continental shelf of the southern Weddell Sea, Antarctica: A review. *Rev. Geophys.,* **47,** RG3003, doi:10.1029/2007RG000250.

Niiler, P., and E. B. Kraus, 1977: One-dimensional models of the upper ocean. *Modeling and Prediction of the Upper Layers of the Ocean,* E. B. Kraus, Ed., Pergamon Press, 143–172.

Orsi, A. H., and C. L. Wiederwohl, 2009: A recount of Ross Sea waters. *Deep-Sea Res.,* **56,** 778–795, doi:10.1016/j.dsr2.2008.10.033.

——, G. Johnson, and J. Bullister, 1999: Circulation, mixing, and production of Antarctic Bottom Water. *Prog. Oceanogr.,* **43,** 55–109.

Pollard, D., M. Batteen, and Y. Han, 1983: Development of a simple upper-ocean and sea-ice model. *J. Phys. Oceanogr.,* **13,** 754–767.

Price, J. F., R. A. Weller, and R. Pinkel, 1986: Diurnal cycling: Observations and models of the upper ocean response to diurnal heating, cooling, and wind mixing. *J. Geophys. Res.,* **91** (C7), 8411–8427.

Pritchard, H. D., R. J. Arthern, D. G. Vaughan, and L. A. Edwards, 2009: Extensive dynamic thinning on the margins of the Greenland and Antarctic ice sheets. *Nature,* **461,** 971–975.

Renfrew, I. A., J. C. King, and T. Markus, 2002: Coastal polynyas in the southern Weddell Sea: Variability of the surface energy budget. *J. Geophys. Res.,* **107,** 3063, doi:10.1029/2000JC000720.

Saha, S., and Coauthors, 2006: The NCEP Climate Forecast System. *J. Climate,* **19,** 3483–3517.

Semtner, A. J., 1976: A model for the thermodynamic growth of sea ice in numerical investigations of climate. *J. Phys. Oceanogr.,* **6,** 379–389.

Shepherd, A., D. Wingham, and E. Rignot, 2004: Warm ocean is eroding West Antarctic Ice Sheet. *Geophys. Res. Lett.,* **31,** L23402, doi:10.1029/2004GL021106.

Steele, M., 1992: Sea ice melting and floe geometry in a simple ice-ocean model. *J. Geophys. Res.,* **97** (C11), 17 729–17 738.

Talbot, M. H., 1988: Oceanic environment of George VI Ice Shelf, Antarctic Peninsula. *Ann. Glaciol.,* **11,** 161–164.

Tang, C. L., 1991: A two-dimensional thermodynamic model for sea ice advance and retreat in the Newfoundland marginal ice zone. *J. Geophys. Res.,* **96** (C3), 4723–4737.

——, and B. M. DeTracey, 1998: Space-time variation of mixed-layer properties, heat and salt fluxes, and ice melt in the newfoundland marginal ice zone. *J. Geophys. Res.,* **103** (C1), 1177–1191.

Taylor, P. D., and D. L. Feltham, 2004: A model of melt pond evolution on sea ice. *J. Geophys. Res.,* **109,** C12007, doi:10.1029/2004JC002361.

Thoma, M., A. Jenkins, D. Holland, and S. Jacobs, 2008: Modelling Circumpolar Deep Water intrusions on the Amundsen sea continental shelf, Antarctica. *Geophys. Res. Lett.,* **35,** L18602, doi:10.1029/2008GL034939.

Timmermann, R., and A. Beckmann, 2004: Parameterization of vertical mixing in the Weddell Sea. *Ocean Modell.,* **6,** 83–100.

——, and M. Losch, 2005: Erratum: Using the Mellor-Yamada mixing scheme in seasonally ice-covered seas—corrigendum to: Parameterization of vertical mixing in the Weddell Sea. *Ocean Modell.,* **6,** 83–100, doi:10.1016/S1463-5003(02)00061-6.

——, and Coauthors, 2010: A consistent dataset of Antarctic ice sheet topography, cavity geometry, and global bathymetry. *Earth Syst. Sci. Data Discuss.,* **3,** 231–257.

UNESCO, 1981: Background papers supporting data on the international equation of state of seawater 1980. UNESCO Tech. Paper in Marine Science 38, 192 pp.

van den Broeke, M., W. J. van de Berg, and E. van Meijgaard, 2006: Snowfall in coastal West Antarctica much greater than previously assumed. *Geophys. Res. Lett.,* **33,** L02505, doi:10.1029/2005GL025239.

van Lipzig, N. P. M., J. Turner, S. R. Colwell, and M. R. van Den Broeke, 2004: The near-surface wind field over the antarctic continent. *Int. J. Climatol.,* **24,** 1973–1982, doi:10.1002/joc.1090.

Wåhlin, A. K., X. Yuan, G. Björk, and C. Nohr, 2010: Inflow of warm Circumpolar Deep Water in the central Amundsen shelf. *J. Phys. Oceanogr.,* **40,** 1427–1434.

Walker, D. P., M. A. Brandon, A. Jenkins, J. T. Allen, J. A. Dowdeswell, and J. Evans, 2007: Oceanic heat transport onto the Amundsen sea shelf through a submarine glacial trough. *Geophys. Res. Lett.,* **34,** L02602, doi:10.1029/2006GL028154.

Wilchinsky, A. V., and D. L. Feltham, 2009: Numerical simulation of the Filchner overflow. *J. Geophys. Res.,* **114,** C12012, doi:10.1029/2008JC005013.

Worby, A. P., C. A. Geiger, M. J. Paget, M. L. Van Woert, S. F. Ackley, and T. L. DeLiberty, 2008: Thickness distribution of Antarctic sea ice. *J. Geophys. Res.,* **113,** C05S92, doi:10.1029/2007JC004254.